Degenerate four-wave mixing in nonlinear resonators comprising two-dimensional materials: A coupled-mode theory approach

Thomas Christopoulos,[1,*] Odysseas Tsilipakos,[2] Georgios Sinatkas,[1] and Emmanouil E. Kriezis[1]

[1]*School of Electrical and Computer Engineering, Aristotle University of Thessaloniki (AUTH), Thessaloniki 54124, Greece*
[2]*Institute of Electronic Structure and Laser, Foundation for Research and Technology Hellas (FORTH), Heraklion 71110, Crete, Greece*

Two-dimensional (2D) or sheet materials have been recently recognized as fascinating materials for nonlinear photonics. Here, we develop a rigorous mathematical framework based on perturbation theory and temporal coupled-mode theory capable of analyzing third-order, $\chi^{(3)}$, multichannel nonlinear processes in resonant systems comprising 2D materials. The framework is applied to model degenerate four-wave mixing in a guided-wave graphene plasmon-polariton resonant structure, consisting of a standing-wave resonator directly coupled to access waveguides. The results obtained with the proposed framework are compared with full-wave finite-element simulations revealing excellent agreement. Aside from being accurate and efficient, our framework allows for selectively incorporating different nonlinear phenomena, identifying their unique impact on the nonlinear response and providing valuable physical insight. We are, thus, able to specify the optimal operating point leading to maximum conversion efficiency for the generated wave in a multiparameter space. In addition, we identify unstable operating regimes exhibiting optical bistability or limit cycles, thoroughly characterizing the component performance. Our framework enables the study of diverse multichannel phenomena (frequency generation, frequency mixing, and parametric amplification) in the thriving field of 2D material photonics, thus allowing for assessing the potential of these exciting materials for practical nonlinear applications.

DOI: 10.1103/PhysRevB.98.235421

I. INTRODUCTION

Four-wave mixing (FWM) and its more popular variant, degenerate four-wave mixing (DFWM), which entails the interaction of two input waves, are invaluable third-order, $\chi^{(3)}$, nonlinear processes for obtaining efficient frequency mixing, achieving parametric amplification of an existing wave, or generating optical frequency combs. First observed theoretically and experimentally in nonlinear optical fibers [1], FWM has also witnessed a surge of activity in nanophotonic waveguide structures [2–4] and resonant systems [5,6]. Especially in the latter, FWM has gathered considerable attention due to the intensity buildup allowing for high conversion efficiency with moderate input power, their small footprint (especially ring resonators), and the fact that the phase-matching condition can be inherently satisfied by the resonator spectrum. Realizations in a variety of photonic platforms have been successfully demonstrated with standard manufacturing techniques and monolithic integration [7–11].

Thus far, mainly bulk nonlinear materials have been incorporated in resonator structures to introduce nonlinearity. In resonant systems with bulk nonlinearity, multichannel processes, such as second- and third-harmonic generation, and degenerate four-wave mixing, can be efficiently studied with a coupled-mode theory (CMT) framework, as shown with photonic crystal structures [11–15]. However, atomically thin 2D materials (most notably graphene [16], transition metal dichalcogenides [17], hexagonal boron nitride [18],

black phosphorus [19], etc.) have been recently recognized as fascinating materials for photonics and nonlinear applications [20]. In fact, the most popular 2D material, graphene, has been examined for harmonic frequency generation and wave mixing in free-space photonics [21–24], revealing its highly nonlinear electromagnetic response in combination with its unique linear properties [25–28]. Capitalizing on the capability of integrating and dynamically controlling graphene in photonic chips [29], theoretical and experimental works have recently appeared in the literature demonstrating guided-wave components, spanning from graphene-covered waveguides [30,31] to graphene-covered photonic crystal resonators [32] and silicon rings [33], all focusing on the manifestation of efficient four-wave mixing enabled by the extreme nonlinearity of graphene. Still, an efficient and flexible numerical tool that can model multichannel nonlinear processes in resonant structures comprising 2D materials is missing from the literature.

In this work, we construct a strict mathematical framework that can accurately and efficiently analyze frequency generation and wave-mixing phenomena in such structures, allowing to obtain useful design rules and physical insight. Our framework is based on perturbation theory and coupled-mode theory, in direct analogy with our previous works on single-channel phenomena like self-phase modulation (SPM), two-photon absorption, optical bistability, and saturable absorption [34–36]. It allows for treating 2D materials as infinitesimally thin, avoiding erroneous results associated with effective bulk material representations. Importantly, we also take into account material dispersion in the linear properties since graphene, for example, is highly dispersive, which has

*cthomasa@ece.auth.gr

been proven to significantly affect the linear and nonlinear response of resonant devices [34].

Using a simple, yet representative, example of a graphene-based standing-wave resonator in the THz frequency band, we highlight the accuracy of the developed framework by comparing with full-wave simulations. Furthermore, we elegantly use CMT to identify the optimal operating point leading to maximum conversion efficiency in a multiparametric space, paving the way for the design of more advanced photonic resonant devices. Finally, the capability of the framework to treat system instabilities, such as optical bistability and limit cycles, is demonstrated as part of the thorough device performance analysis.

II. MULTICHANNEL THEORETICAL FRAMEWORK FOR NONLINEAR RESONATORS COMPRISING 2D MATERIALS

We first construct a theoretical framework capable of handling multichannel nonlinear processes in resonant structures comprising bulk and sheet nonlinear materials. The framework is based on two pillars: perturbation theory [37] and temporal coupled-mode theory [38,39]. It combines a number of advantageous characteristics: it is highly accurate, it is computationally efficient, it allows for incorporating diverse nonlinear phenomena as well as studying a multitude of nonlinear processes, and it captures in depth the underlying physics providing valuable physical insight.

A. Perturbation theory for resonators with nonlinear 2D materials

In resonant structures with relatively weak nonlinearities, perturbation theory can be used to estimate the effect of nonlinearity on the resonance characteristics (resonance frequency, quality factor) of the cavity [37]. In the case of a single cavity comprising bulk and sheet (2D) nonlinear materials, the nonlinear frequency shift of a d-dimensional system is given by [34]

$$\frac{\Delta\omega}{\omega_0} = -\frac{\int \mathbf{P}_{\text{NL}} \cdot \mathbf{E}_0^* d^d r - j\frac{1}{\omega_0}\int \mathbf{J}_{\text{NL}} \cdot \mathbf{E}_0^* d^{d-1} r}{\int \varepsilon_0 \frac{\partial\{\omega\overline{\varepsilon}_r(\omega)\}}{\partial\omega}\mathbf{E}_0 \cdot \mathbf{E}_0^* d^d r + \int \mu_0 \mathbf{H}_0 \cdot \mathbf{H}_0^* d^d r + \int \frac{\partial\overline{\sigma}_{\text{Im}}^{(1)}(\omega)}{\partial\omega}\mathbf{E}_0 \cdot \mathbf{E}_0^* d^{d-1} r}, \quad (1)$$

where $\Delta\omega$ is, in general, complex, incorporating the effect of nonlinear losses. In Eq. (1), $\mathbf{P}_{\text{NL}}$ stands for the nonlinear polarization, corresponding to dielectric bulk nonlinearities, and $\mathbf{J}_{\text{NL}}$ for the nonlinear surface current density. Both terms can be exploited to model single-channel effects (self-phase modulation, optical bistability, self-pulsation) as well as multichannel processes such as cross-phase modulation (XPM), third-harmonic generation (THG), and four-wave mixing. The $\mathbf{J}_{\text{NL}}$ term allows for naturally treating conductive nonlinear 2D materials, such as graphene. In addition, the denominator in Eq. (1) is proportional to the stored energy in the cavity. It comprises dispersive electric energy and magnetic energy terms as well as an extra term representing the energy stored in the surface current density due to the dispersive imaginary part of the electrical conductivity [34]. This term is important when highly dispersive conductive materials are considered such as graphene in the THz.

To specifically introduce SPM, XPM, and DFWM in the framework, we assume three waves with frequencies ω_1, ω_2, and $\omega_3 = 2\omega_1 - \omega_2$ (frequency-matching condition) and seek the third-order nonlinear polarization and surface current density terms in the time domain

$$\mathcal{P}_{\text{NL}} = \varepsilon_0 \overline{\chi}^{(3)} \mid \mathcal{E}\mathcal{E}\mathcal{E}, \quad (2a)$$

$$\mathcal{J}_{\text{NL}} = \overline{\sigma}^{(3)} \mid \mathcal{E}\mathcal{E}\mathcal{E}. \quad (2b)$$

The tensorial nature of the linear relative permittivity and linear electrical conductivity is hereafter omitted by replacing the superscripts in the notation with the respective subscripts. As a result, the presented analysis stands for isotropic bulk and isotropic 2D materials that solely interact with the tangential electric field components: $\mathbf{J}_k = (\sigma_{1,\text{Re}} + j\sigma_{1,\text{Im}})\mathbf{E}_{k,\parallel}$.

To proceed, we substitute $\mathcal{E} = \text{Re}\{\mathbf{E}_1 \exp(j\omega_1 t) + \mathbf{E}_2 \exp(j\omega_2 t) + \mathbf{E}_3 \exp(j\omega_3 t)\}$ in Eqs. (2). In the frequency domain, the nonlinear surface current density, in the general case, can be expressed as

$$J_{\text{NL},\mu}(\omega_k + \omega_\ell + \omega_m) = \frac{1}{4}\sum_{\alpha\beta\gamma} \sigma_{\mu\alpha\beta\gamma}^{(3)} E_{k,\alpha} E_{\ell,\beta} E_{m,\gamma}, \quad (3)$$

where $k, \ell, m = \{1, 2, 3\}$ and $\mu, \alpha, \beta, \gamma = \{x, y, z\}$. In case of negative frequencies in Eq. (3), the respective electric field component should be replaced by its complex conjugate, i.e., $-\omega_k \leftrightarrow E_{k,\alpha}^*$. A similar equation stands for the nonlinear polarization term, not presented for brevity.

In the most common approach which is also the one examined here, polarization nonlinearities are assumed isotropic $[\chi_{\mu\alpha\beta\gamma}^{(3)} = \chi_3(\delta_{\mu\alpha}\delta_{\beta\gamma} + \delta_{\mu\beta}\delta_{\alpha\gamma} + \delta_{\mu\gamma}\delta_{\alpha\beta})/3]$, while the equivalent isotropic condition is applied for the nonlinear surface current density of the nonlinear 2D material $[\sigma_{\mu\alpha\beta\gamma}^{(3)} = \sigma_3(\delta_{\mu\alpha}\delta_{\beta\gamma} + \delta_{\mu\beta}\delta_{\alpha\gamma} + \delta_{\mu\gamma}\delta_{\alpha\beta})/3$, with $\mu, \alpha, \beta, \gamma$ restricted to the tangential directions and $\delta_{\mu\alpha}$ standing for the Kronecker delta] [28,40,41]. Then, the nonlinear current density terms are expressed as

$$\mathbf{J}_{\text{NL}}(\omega_k) = \mathbf{J}_{\text{SPM}}(\omega_k) + \mathbf{J}_{\text{XPM}}(\omega_k) + \mathbf{J}_{\text{DFWM}}(\omega_k). \quad (4)$$

The nonlinear currents due to SPM ($\omega_k = \omega_k - \omega_k + \omega_k$) and XPM ($\omega_k = \omega_k - \omega_\ell + \omega_\ell = \omega_k - \omega_m + \omega_m$) are calculated

equal to

$$\mathbf{J}_{\text{SPM}}(\omega_k) = \tfrac{1}{4}\sigma_3[2(\mathbf{E}_{k,\parallel} \cdot \mathbf{E}^*_{k,\parallel})\mathbf{E}_{k,\parallel} + (\mathbf{E}_{k,\parallel} \cdot \mathbf{E}_{k,\parallel})\mathbf{E}^*_{k,\parallel}], \tag{5a}$$

$$\mathbf{J}_{\text{XPM}}(\omega_k) = \tfrac{1}{4}\sigma_3[2(\mathbf{E}_{\ell,\parallel} \cdot \mathbf{E}^*_{\ell,\parallel})\mathbf{E}_{k,\parallel} + 2(\mathbf{E}_{k,\parallel} \cdot \mathbf{E}_{\ell,\parallel})\mathbf{E}^*_{\ell,\parallel} + 2(\mathbf{E}_{k,\parallel} \cdot \mathbf{E}^*_{\ell,\parallel})\mathbf{E}_{\ell,\parallel}]$$
$$+ \tfrac{1}{4}\sigma_3[2(\mathbf{E}_{m,\parallel} \cdot \mathbf{E}^*_{m,\parallel})\mathbf{E}_{k,\parallel} + 2(\mathbf{E}_{k,\parallel} \cdot \mathbf{E}_{m,\parallel})\mathbf{E}^*_{m,\parallel} + 2(\mathbf{E}_{k,\parallel} \cdot \mathbf{E}^*_{m,\parallel})\mathbf{E}_{m,\parallel}]. \tag{5b}$$

Furthermore, new waves are generated in all three frequencies $\omega_1 = -\omega_1 + \omega_2 + \omega_3$, $\omega_2 = 2\omega_1 - \omega_3$, and $\omega_3 = 2\omega_1 - \omega_2$ due to paired nonlinear interactions, expressed in the here examined conventional DFWM as

$$\mathbf{J}_{\text{DFWM}}(\omega_1) = \tfrac{1}{4}\sigma_3[2(\mathbf{E}_{2,\parallel} \cdot \mathbf{E}_{3,\parallel})\mathbf{E}^*_{1,\parallel} + 2(\mathbf{E}^*_{1,\parallel} \cdot \mathbf{E}_{3,\parallel})\mathbf{E}_{2,\parallel} + 2(\mathbf{E}^*_{1,\parallel} \cdot \mathbf{E}_{2,\parallel})\mathbf{E}_{3,\parallel}], \tag{6a}$$

$$\mathbf{J}_{\text{DFWM}}(\omega_2) = \tfrac{1}{4}\sigma_3[2(\mathbf{E}_{1,\parallel} \cdot \mathbf{E}^*_{3,\parallel})\mathbf{E}_{1,\parallel} + (\mathbf{E}_{1,\parallel} \cdot \mathbf{E}_{1,\parallel})\mathbf{E}^*_{3,\parallel}], \tag{6b}$$

$$\mathbf{J}_{\text{DFWM}}(\omega_3) = \tfrac{1}{4}\sigma_3[2(\mathbf{E}_{1,\parallel} \cdot \mathbf{E}^*_{2,\parallel})\mathbf{E}_{1,\parallel} + (\mathbf{E}_{1,\parallel} \cdot \mathbf{E}_{1,\parallel})\mathbf{E}^*_{2,\parallel}]. \tag{6c}$$

The respective polarization terms have entirely similar expressions, not presented here for brevity, with the tangential electric field being replaced by the full field vector.

By substituting Eqs. (5), (6), and the respective polarization terms in Eq. (1), we can calculate the full nonlinear frequency shift $\Delta\omega_k$, experienced by the three resonance modes ω_1, ω_2, and ω_3, that SPM, XPM, and DFWM effects introduce

$$\Delta\omega_1 a_1 = -\gamma_{11}|a_1|^2 a_1 - 2\gamma_{12}|a_2|^2 a_1 - 2\gamma_{13}|a_3|^2 a_1 - 2\beta_1 a_1^* a_2 a_3, \tag{7a}$$

$$\Delta\omega_2 a_2 = -\gamma_{22}|a_2|^2 a_2 - 2\gamma_{21}|a_1|^2 a_2 - 2\gamma_{23}|a_3|^2 a_2 - \beta_2 a_1^2 a_3^*, \tag{7b}$$

$$\Delta\omega_3 a_3 = -\gamma_{33}|a_3|^2 a_3 - 2\gamma_{31}|a_1|^2 a_3 - 2\gamma_{32}|a_2|^2 a_3 - \beta_3 a_1^2 a_2^*, \tag{7c}$$

where a_k is the resonance amplitude, normalized so that $|a_k|^2 \equiv W_{\text{res},k}$ represents the energy stored in the cavity. To obtain Eqs. (7), the normalizations $\mathbf{E}_k \to \mathbf{E}_k a_k(t)/\sqrt{W_{\text{res},k}}$ and $\mathbf{H}_k \to \mathbf{H}_k a_k(t)/\sqrt{W_{\text{res},k}}$ are introduced [12]. The nonlinear coefficients $\gamma_{k\ell}$ and β_k (including both bulk and sheet contributions), describing SPM/XPM and FWM effects, respectively, are given by

$$\gamma_{k\ell} = 4\left(\frac{\omega_k}{c_0}\right)^d \omega_k c_0 \kappa_{k\ell,b} n_2^{\text{max}} + \left(\frac{\omega_k}{c_0}\right)^{d+1} \kappa_{k\ell,s} \frac{\sigma_{3,\text{Im}}^{\text{max}}}{\varepsilon_0^2}, \tag{8a}$$

$$\beta_k = 4\left(\frac{\omega_k}{c_0}\right)^d \omega_k c_0 \kappa_{k,b}^{\text{DFWM}} n_2^{\text{max}} + \left(\frac{\omega_k}{c_0}\right)^{d+1} \kappa_{k,s}^{\text{DFWM}} \frac{\sigma_{3,\text{Im}}^{\text{max}}}{\varepsilon_0^2}, \tag{8b}$$

with the dimensionless nonlinear feedback parameters for bulk materials [14,34,39,42] calculated through

$$\kappa_{kk,b} = \left(\frac{c_0}{\omega_k}\right)^d \frac{\frac{1}{3}\int n^2 n_2 (2|\mathbf{E}_k|^4 + |\mathbf{E}_k \cdot \mathbf{E}_k|^2) d^d r}{\frac{16}{\varepsilon_0^2} W_{\text{res},k}^2 n_2^{\text{max}}}, \tag{9a}$$

$$\kappa_{k\ell,b} = \left(\frac{c_0}{\omega_k}\right)^d \frac{\frac{1}{3}\int n^2 n_2 (|\mathbf{E}_k|^2 |\mathbf{E}_\ell|^2 + |\mathbf{E}_k \cdot \mathbf{E}_\ell|^2 + |\mathbf{E}_k \cdot \mathbf{E}_\ell^*|^2) d^d r}{\frac{16}{\varepsilon_0^2} W_{\text{res},k} W_{\text{res},\ell} n_2^{\text{max}}}, \tag{9b}$$

$$\kappa_{1,b}^{\text{DFWM}} = \left(\frac{c_0}{\omega_1}\right)^d \frac{\frac{1}{3}\int n^2 n_2 [2(\mathbf{E}_1^* \cdot \mathbf{E}_3)(\mathbf{E}_1^* \cdot \mathbf{E}_2) + (\mathbf{E}_1^* \cdot \mathbf{E}_1^*)(\mathbf{E}_2 \cdot \mathbf{E}_3)] d^d r}{\frac{16}{\varepsilon_0^2} W_{\text{res},1} W_{\text{res},2}^{1/2} W_{\text{res},3}^{1/2} n_2^{\text{max}}}, \tag{9c}$$

and for sheet materials through

$$\kappa_{kk,s} = \left(\frac{c_0}{\omega_k}\right)^{d+1} \frac{\int \sigma_{3,\text{Im}} (2|\mathbf{E}_{k,\parallel}|^4 + |\mathbf{E}_{k,\parallel} \cdot \mathbf{E}_{k,\parallel}|^2) d^{d-1} r}{\frac{16}{\varepsilon_0^2} W_{\text{res},k}^2 \sigma_{3,\text{Im}}^{\text{max}}}, \tag{10a}$$

$$\kappa_{k\ell,s} = \left(\frac{c_0}{\omega_k}\right)^{d+1} \frac{\int \sigma_{3,\text{Im}} (|\mathbf{E}_{k,\parallel}|^2 |\mathbf{E}_{\ell,\parallel}|^2 + |\mathbf{E}_{k,\parallel} \cdot \mathbf{E}_{\ell,\parallel}|^2 + |\mathbf{E}_{k,\parallel} \cdot \mathbf{E}_{\ell,\parallel}^*|^2) d^{d-1} r}{\frac{16}{\varepsilon_0^2} W_{\text{res},k} W_{\text{res},\ell} \sigma_{3,\text{Im}}^{\text{max}}}, \tag{10b}$$

$$\kappa_{1,s}^{\text{DFWM}} = \left(\frac{c_0}{\omega_1}\right)^{d+1} \frac{\int \sigma_{3,\text{Im}}[2(\mathbf{E}_{1,\parallel}^* \cdot \mathbf{E}_{3,\parallel})(\mathbf{E}_{1,\parallel}^* \cdot \mathbf{E}_{2,\parallel}) + (\mathbf{E}_{1,\parallel}^* \cdot \mathbf{E}_{1,\parallel}^*)(\mathbf{E}_{2,\parallel} \cdot \mathbf{E}_{3,\parallel})]d^{d-1}r}{\frac{16}{\varepsilon_0^2}W_{\text{res},1}W_{\text{res},2}^{1/2}W_{\text{res},3}^{1/2}\sigma_{3,\text{Im}}^{\text{max}}}. \tag{10c}$$

The SPM contribution is enclosed in the κ_{kk} nonlinear feedback parameters, while XPM is described by $\kappa_{k\ell}$ and DFWM by κ_k^{DFWM}. Two-photon absorption (TPA) is considered negligible at THz frequencies. It is important to note that $\kappa_{k\ell}$ are by definition real [resulting also in real $\gamma_{k\ell}$ in the absence of nonlinear losses, which is the case of Eq. (8)]; however, κ_k^{DFWM} (β_k) are in general complex. Furthermore, it holds that

$$\kappa_{1,b}^{\text{DFWM}} = \left(\frac{\omega_2}{\omega_1}\right)^d (\kappa_{2,b}^{\text{DFWM}})^* = \left(\frac{\omega_3}{\omega_1}\right)^d (\kappa_{3,b}^{\text{DFWM}})^*, \tag{11a}$$

$$\kappa_{1,s}^{\text{DFWM}} = \left(\frac{\omega_2}{\omega_1}\right)^{d+1} (\kappa_{2,s}^{\text{DFWM}})^* = \left(\frac{\omega_2}{\omega_1}\right)^{d+1} (\kappa_{3,s}^{\text{DFWM}})^*, \tag{11b}$$

for bulk and sheet materials, respectively. The aforementioned equalities are reflected in the nonlinear DFWM parameters β_k, i.e., it holds,

$$\frac{\beta_{1,b}}{\omega_1} = \frac{\beta_{2,b}^*}{\omega_2} = \frac{\beta_{3,b}^*}{\omega_3}, \tag{12a}$$

$$\beta_{1,s} = \beta_{2,s}^* = \beta_{3,s}^*. \tag{12b}$$

Finally, the stored energy in the cavity at each frequency consists of three terms [34] and is given by

$$W_{\text{res},k} = \frac{1}{4}\int \frac{\partial\{\omega\varepsilon_0\varepsilon_r\}}{\partial\omega}\bigg|_{\omega=\omega_k}|\mathbf{E}_k|^2 d^d r + \frac{1}{4}\int \mu_0|\mathbf{H}_k|^2 d^d r + \frac{1}{4}\int \frac{\partial\sigma_{1,\text{Im}}}{\partial\omega}\bigg|_{\omega=\omega_k}|\mathbf{E}_{k,\parallel}|^2 d^{d-1}r. \tag{13}$$

B. Multichannel temporal coupled-mode theory

The nonlinear resonance frequency shifts $\Delta\omega_k$ in Eqs. (7) can be readily incorporated in the CMT framework. Assuming that the three examined frequencies lie in the vicinity of three separate resonances of a directly coupled standing-wave cavity, we can write the amplitude rate equations as

$$\frac{da_1}{dt} = j(\omega_1 - \gamma_{11}|a_1|^2 - 2\gamma_{12}|a_2|^2 - 2\gamma_{13}|a_3|^2)a_1 - j2\beta_1 a_1^* a_2 a_3 - \left(\frac{1}{\tau_{i,1}} + \frac{1}{\tau_{e,1}}\right)a_1 + \sqrt{\frac{1}{\tau_{e,1}}}s_{\text{in},1}, \tag{14a}$$

$$\frac{da_2}{dt} = j(\omega_2 - 2\gamma_{21}|a_1|^2 - \gamma_{22}|a_2|^2 - 2\gamma_{23}|a_3|^2)a_2 - j\beta_2 a_1^2 a_3^* - \left(\frac{1}{\tau_{i,2}} + \frac{1}{\tau_{e,2}}\right)a_2 + \sqrt{\frac{1}{\tau_{e,2}}}s_{\text{in},2}, \tag{14b}$$

$$\frac{da_3}{dt} = j(\omega_3 - 2\gamma_{31}|a_1|^2 - 2\gamma_{32}|a_3|^2 - \gamma_{33}|a_3|^2)a_3 - j\beta_3 a_1^2 a_2^* - \left(\frac{1}{\tau_{i,3}} + \frac{1}{\tau_{e,3}}\right)a_3 + \sqrt{\frac{1}{\tau_{e,3}}}s_{\text{in},3}, \tag{14c}$$

where τ_i, τ_e are the cavity photon lifetimes corresponding to intrinsic (resistive and radiation) and external (coupling) loss, with the respective quality factors given by $Q = \omega\tau/2$. In addition, the output (transmitted) and reflected waves are calculated through [43]

$$s_{\text{out},k} = \sqrt{\frac{1}{\tau_{e,k}}}a_k, \tag{15a}$$

$$s_{\text{ref},k} = -s_{\text{in},k} + \sqrt{\frac{1}{\tau_{e,k}}}a_k, \tag{15b}$$

respectively, where s are normalized so that $|s|^2$ expresses the guided power. Other type of resonators and/or coupling schemes may be easily incorporated by using the appropriate driving term s_{in} and the corresponding equation for the output waves [38]. The temporal CMT framework of Eqs. (14) describes the temporal evolution of the stored energy in a resonant system. In straight analogy, there is a spatial CMT framework, where space is the dynamic parameter instead of time, which can describe the spatial evolution of the guided power in guided-wave systems. Such a framework has been proposed in Ref. [30] for graphene-comprising, silicon-based waveguides.

Typically, no input wave is introduced in DFWM at the generated frequency ω_3, i.e., $s_{\text{in},3} = 0$. Nevertheless, we include this parameter in the CMT equations to allow for the general case, also referred to as parametric amplification. Furthermore, we note that for an uncoupled and lossless system after ignoring SPM and XPM, the conservation of energy in Eqs. (14) yields

$$2\beta_1 = \beta_2^* + \beta_3^*. \tag{16}$$

Since losses, SPM, and XPM are independent of DFWM, Eq. (16) still holds for the full nonlinear system. This is also

confirmed by the definitions of the nonlinear parameters β_k, Eqs. (8)–(10).

Equations (14) and (15) are usually normalized with respect to the phenomenon under study. Here, we choose to normalize with respect to the $\beta_3 a_1^2 a_2^*$ term [44], i.e., the result of the DFWM process. Thus, we define

$$\tilde{u}_k = \sqrt{\tau_{e,3}|\beta_3|}\,\tilde{a}_k, \tag{17a}$$

$$\tilde{\psi}_k = \sqrt{\tau_{e,3}^2|\beta_3|}\,\tilde{s}_k. \tag{17b}$$

and $t' = t/\tau_{e,3}$, while we let $a_k(t) = \tilde{a}_k(t)\exp\{j\omega_k^{\mathrm{op}}t\}$ and $s_k(t) = \tilde{s}_k(t)\exp\{j\omega_k^{\mathrm{op}}t\}$, marking with ω_k^{op} the operating frequency of the kth wave that is in general different from the respective resonance frequency of the cavity; obviously, $\omega_3^{\mathrm{op}} = 2\omega_1^{\mathrm{op}} - \omega_2^{\mathrm{op}}$, as dictated by the mixing process. The above normalization implies that the input/output wave power is normalized with respect to the *characteristic power*

$$P_3 = \frac{1}{\tau_{e,3}^2|\beta_3|} \tag{18}$$

of the system. The normalization eventually leads to

$$\frac{\tau_{e,k}}{\tau_{e,3}}\frac{d\tilde{u}_k}{dt'} = j(-\delta_k - r_{\mathrm{SPM},k}|\tilde{u}_k|^2 - r_{\mathrm{XPM},k\ell}|\tilde{u}_\ell|^2 - r_{\mathrm{XPM},km}|\tilde{u}_m|^2)\tilde{u}_k - jr_{\mathrm{DFWM},k}\Phi_k(\tilde{u}_1,\tilde{u}_2,\tilde{u}_3) - (1 + r_{Q,k})\tilde{u}_k + \sqrt{\frac{\tau_{e,k}}{\tau_{e,3}}}\tilde{\psi}_{\mathrm{in},k}, \tag{19a}$$

$$\tilde{\psi}_{\mathrm{out},k} = \sqrt{\frac{\tau_{e,3}}{\tau_{e,k}}}\tilde{u}_k, \tag{19b}$$

$$\tilde{\psi}_{\mathrm{ref},k} = -\tilde{\psi}_{\mathrm{in},k} + \sqrt{\frac{\tau_{e,3}}{\tau_{e,k}}}\tilde{u}_k. \tag{19c}$$

The normalization parameters appearing in Eqs. (19) are as follows:

(i) the resonance frequency detuning $\delta_k = (\omega_k^{\mathrm{op}} - \omega_k)\tau_{e,k}$,

(ii) the quality factor ratio $r_{Q,k} = \tau_{e,k}/\tau_{i,k}$,

(iii) the SPM intensity ratio $r_{\mathrm{SPM},k} = \gamma_{kk}\tau_{e,k}/(|\beta_3|\tau_{e,3})$,

(iv) the XPM intensity ratio $r_{\mathrm{XPM},k\ell} = 2\gamma_{k\ell}\tau_{e,k}/(|\beta_3|\tau_{e,3})$,

(v) the DFWM intensity ratio $r_{\mathrm{DFWM},k} = \beta_k\tau_{e,k}/(|\beta_3|\tau_{e,3})$.

Note that $r_{\mathrm{DFWM},3} \neq 1$, in contrast to what one might expect, since this parameter quantifies the contribution of both the real and imaginary parts of β_3. Nevertheless, it turns out that only the absolute value of $r_{\mathrm{DFWM},3}$ (which always equals unity) affects the intensity of the produced wave. Finally, we have introduced for brevity the function $\Phi_k(\tilde{u}_1,\tilde{u}_2,\tilde{u}_3)$, defined as

$$\Phi_k(\tilde{u}_1,\tilde{u}_2,\tilde{u}_3) = \begin{cases} 2\tilde{u}_1^*\tilde{u}_2\tilde{u}_3, & k=1 \\ \tilde{u}_1^2\tilde{u}_3^*, & k=2 \\ \tilde{u}_1^2\tilde{u}_2^*, & k=3. \end{cases} \tag{20}$$

III. DEGENERATE FOUR-WAVE MIXING IN A GRAPHENE PLASMON-POLARITON RESONATOR

Next, we utilize the developed framework to study degenerate four-wave mixing in a graphene-based standing-wave resonator in the THz band. The resonator is formed by an infinitely wide graphene strip of length L, coupled with two graphene sheets, serving as the feeding waveguides, through coupling gaps of length g (Fig. 1). Due to the uniformity along the z axis, the structure is studied using 2D electromagnetic simulations. The linear properties of graphene are modeled using the Kubo formula [28], applied for a Fermi level of $\mu_c = 0.3$ eV, rendering the intraband transitions the sole absorption process due to the low photon energy at THz frequencies. Taking into account the strong Drude-type dispersion of the linear conductivity is essential for correctly estimating the quality factor and the free-spectral range (FSR) of the resonator as well as the extra stored energy due to the surface current [34]

[Eq. (13)]. Note that the nonlinear conductivity of graphene also exhibits dispersion ($\propto \omega^{-3}$) [25,34].

Before utilizing the CMT framework [Eqs. (19)] for studying the nonlinear response, we should specify the coefficients entering in the rate equations, i.e., the linear resonance characteristics of the cavity as well as the nonlinear feedback parameters [Eqs. (10)]. This is performed by conducting linear eigenvalue simulations with the finite element method (FEM) using COMSOL MULTIPHYSICS®. For the proposed structure, we choose to work with high-order modes to limit radiation loss and more specifically the 11th (ω_3, idler), 12th (ω_1, pump), and 13th (ω_2, signal) order modes of an $L = 72$ μm resonator. In Fig. 2, the E_x components of the resonance modes along with the resonance frequencies (lying around 5 THz) and
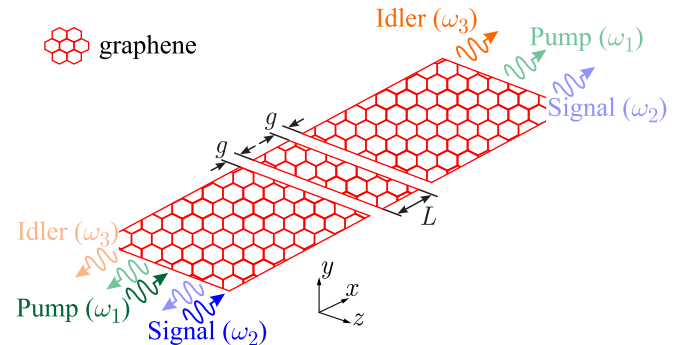
FIG. 1. Graphene plasmon-polariton standing-wave resonator of length L, directly coupled with two semi-infinite graphene sheets, serving as the input/output waveguides through coupling gaps of length g. The nonlinear mixing of signal and pump waves generates a third wave (idler) through the DFWM process. Pale-colored waves carry comparable power with bright-colored waves but they are not presented in any illustration of the paper. In addition, the pale-colored backward propagating idler wave at ω_3 is not accounted for when calculating the conversion efficiency [Eq. (21)].
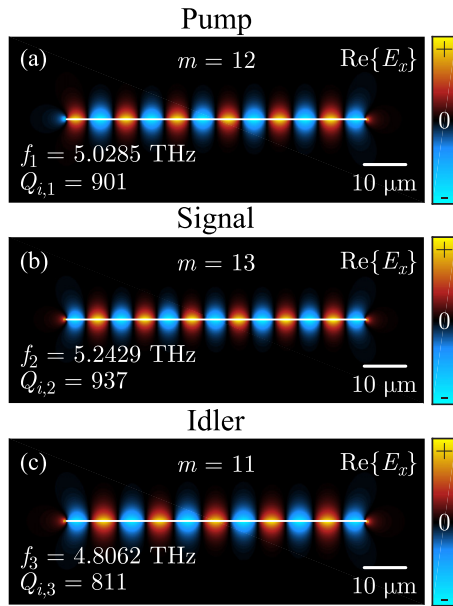
Pump

Signal

Idler

FIG. 2. Field plot (E_x component) of the resonance mode profiles supported by the graphene plasmon-polariton resonator. (a) $m = 12$ (pump wave), (b) $m = 13$ (signal wave), and (c) $m = 11$ (idler wave). It is noted that the three resonance frequencies are not exactly frequency matched ($\omega_3 \neq 2\omega_1 - \omega_2$) due to material dispersion.

FIG. 3. Conversion efficiency of the DFWM process for the depleted (black dashed curve) and the undepleted pump cases (CMT: blue solid curve, FEM: red markers). Depleted and undepleted pump calculations agree well for input powers as high as $p_{in,1} = 1$. CMT and full-wave calculations for the undepleted pump case are in excellent agreement, validating the developed framework. Self- and cross-nonlinear resonance frequency shifts have been neglected ($\gamma_{k\ell} = 0$ in the CMT context).

the respective intrinsic quality factors are depicted. Note that the correct estimation of the intrinsic quality factor is performed by using its definition $Q_{i,k} = \omega_k W_{res,k} / (P_{res,k} + P_{rad,k})$ in a coupled eigenvalue problem, after appropriately limiting the integration domain of the numerator to exclude the energy stored in the bus waveguides and also limiting the integration domain of the denominator to exclude radiation outflow from the waveguides' ports. This calculation is more accurate than using an uncoupled eigenvalue problem to estimate Q_i since a significant part of the radiation couples with the bus waveguide being, after all, part of the coupling (external) loss. Moreover, the energy in the numerator is calculated using Eq. (13) to correctly take into account the dispersion in graphene, which if neglected, would have led to Q factors equal to approximately half of the correct value. Quality factors calculated using this approach result in excellent reconstruction of the Lorentzian-shaped transmission curves obtained by linear time-harmonic simulations. This validates as well that the incident power couples efficiently (without significant radiation leakage from the waveguide) to the resonant mode, i.e., the coupling process between input waveguide and resonator is almost free from scattering losses, something that is attributed to the small coupling gaps and the geometric similarity between their cross sections. Accordingly, the coupling losses are calculated from the same eigenvalue problem using the respective definition $Q_{e,k} = \omega_k W_{res,k} / P_{ext,k}$ and, as expected, depend on the coupling gap g. P_{ext} represents the guided power on both waveguides and is calculated by appropriately integrating the power density of the supported surface-plasmon modes. For $g = 1\ \mu m$, the external quality factors are found equal to $Q_{e,1} = 326$, $Q_{e,2} = 386$, and $Q_{e,3} = 267$, resulting in quality factor ratios $r_{Q,1} = 0.36$, $r_{Q,2} = 0.41$, and $r_{Q,3} = 0.33$, respec-

tively. Since the characteristic power is inversely proportional to the external quality factor, higher-Q_e values (larger gaps) would lead to lower power requirements. Nevertheless, they also lead to higher-r_Q values, suppressing the maximum output on resonance (being optimal for $r_Q = 0$), thus limiting the overall performance. Finally, $\kappa_{3,s}^{DFWM} = 0.3044 + j0.0098$, resulting in a characteristic power of $P_3 = 0.606\ mW/\mu m$.

In order to validate the results obtained with the CMT framework, a second simulation strategy is introduced. Two linear harmonic propagation problems are solved at the resonant frequencies $\omega_1^{op} = \omega_1$ and $\omega_2^{op} = \omega_2$ and the resulting field distributions are used to specify a surface current source term on graphene through Eq. (6c). In turn, this nonlinear source term drives a third time-harmonic propagation simulation at $\omega_3^{op} = 2\omega_1^{op} - \omega_2^{op}$ [23]. In general, $\omega_3^{op} \neq \omega_3$, reflecting a nonideal frequency-matching condition. This can be due to material dispersion, as in our case, waveguide dispersion (when a waveguide cross section with at least one finite dimension is involved) or both, constituting a common problem in FWM resonant photonic circuits [7–9]. Note that this strategy, which we term "full wave" and consists of three *independent* linear full-wave simulations, cannot take into account either the power lost from both pump and signal waves due to frequency conversion or the power generated through the nonlinear interactions between pump-idler and signal-idler waves. Thus, it provides an approximation of the actual system performance, remaining, nevertheless, highly accurate for moderate conversion efficiencies. In the CMT framework, these conditions can be replicated by setting $\beta_1 = \beta_2 = 0$, which consequently violates the energy conservation condition of Eq. (16). We refer to this approximation as the *undepleted pump* case in contrast to the *depleted pump* case where all energy exchange processes are allowed.

In Fig. 3, we plot the conversion efficiency (CE) of the DFWM process defined as

$$\mathrm{CE} = 10 \log \left(\frac{p_{\mathrm{out},3}}{p_{\mathrm{in},1} + p_{\mathrm{in},2}} \right) \qquad (21)$$

for the system under study ($p = |\tilde{\psi}|^2$) and $p_{\mathrm{out},3}$ exclusively refers to the forward-propagating idler. We include both the depleted and undepleted pump scenarios; the depleted pump case is studied with CMT (black dashed curve), while for the undepleted pump case we compare CMT (blue solid line) with the full-wave approach (red markers). Note that the results between the depleted and the undepleted pump case coincide for low conversion efficiencies but start deviating for higher CEs (> -22 dB), as anticipated. A nonmonotonic behavior of the CE curve appears for the depleted pump scenario because as the idler intensity increases, the down-conversion process is boosted, thus setting an upper bound on the achievable conversion efficiency. Importantly, CMT and full-wave approaches are in excellent agreement for the undepleted pump scenario, validating that the proposed framework is capable of accurately modeling the nonlinear response. Finally, let us note that throughout Sec. III the self- and cross-nonlinear resonance frequency shifts arising from the Kerr effect have been neglected ($\gamma_{k\ell} = 0$ in the CMT context), allowing for comparing with the full-wave approach to validate the developed framework. In the next section, we thoroughly study their impact on the conversion efficiency of the DFWM process.

Regarding the device design and performance, $p_{\mathrm{out},3}$ might also be considered as the sum of the power that outflows from both access waveguides. In that case, the total output power at ω_3 is doubled because of the resonator symmetry, equivalently resulting in a 3-dB increase of the conversion efficiency. In an alternative approach, a different system with a single feeding waveguide may be considered; input and output ports will be represented by the same physical waveguide. In that case, although Q_i remains approximately constant (a small reduction is expected because of the extra radiation from the uncoupled edge of the resonator), Q_e and, thus, r_Q are doubled, limiting the observed CE because of the poorer coupling of ω_1 and ω_2 waves. Nevertheless, $P_3 \propto 1/Q_e^2$ is reduced four times with respect to the original system's characteristic power. Changing appropriately the coupling gap g to restore the original value of Q_e leads to CEs comparable to those of the double feed system when considering the idler power flowing both forward and backwards.

IV. IMPACT OF NONLINEAR RESONANCE FREQUENCY SHIFTS AND IDENTIFICATION OF OPERATION REGIMES

In this section, we analyze in depth the performance of the graphene resonator by studying the effect of the nonlinear resonance frequency shifts on the conversion efficiency of the DFWM process. Moreover, we identify different operating regimes, which manifest as the power or the detuning of the input waves is varied. Initially, we seek the optimum power levels for the input waves at ω_1^{op} and ω_2^{op} that lead to the highest CE. For the undepleted pump case, conversion efficiency monotonically increases with input power [Fig. 4(a)], as already seen in Fig. 3. In addition, from Fig. 4(a) one sees

that favoring the ω_1^{op} or ω_2^{op} waves leads to similar CEs. However, the conditions for the undepleted pump approximation do not hold as the CE increases. Opting for the more realistic depleted pump case, there exists an optimal input power pair that leads to maximum CE [Figs. 3 and 4(b)] because of the energy exchange between pump, signal, and idler waves. Using the simple (yet most favorable) conditions $\delta_1 = \delta_2 = 0$ for the operating frequencies of the two input waves (resulting in $\delta_3 = 1.08$ for the produced wave due to graphene conductivity dispersion; waveguide dispersion is absent), we find a CE of -12.5 dB for $P_{\mathrm{in},1} = 7.0 P_3 = 4.242$ mW/μm and $P_{\mathrm{in},2} = 0.5 P_3 = 0.303$ mW/μm [Fig. 4(b)]. The optimal CE point is marked with a star in Fig. 4(b) and lies near the limit
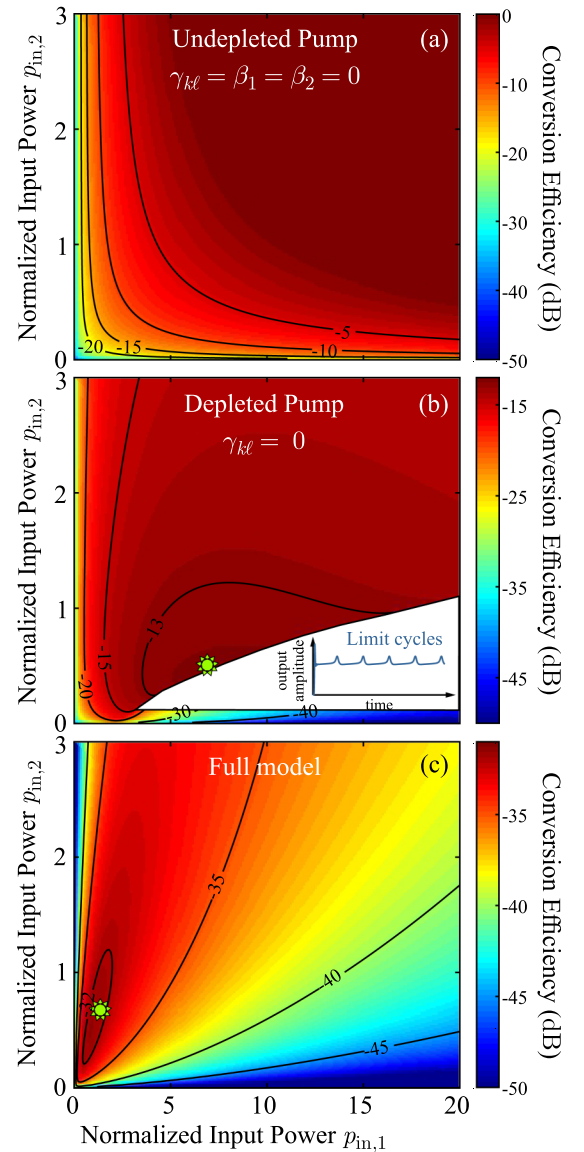
FIG. 4. Conversion efficiency of the DFWM process in the $p_{\mathrm{in},1} - p_{\mathrm{in},2}$ space. (a) Undepleted pump case, (b) depleted pump case, and (c) full model including the nonlinear resonance frequency shifts due to SPM and XPM. In (b) maximum CE (star marker) equals -12.5 dB for $p_{\mathrm{in},1} = 7.0$ and $p_{\mathrm{in},2} = 0.5$. In (c) maximum CE (star marker) equals -31.5 dB for $p_{\mathrm{in},1} = 1.0$ and $p_{\mathrm{in},2} = 0.6$.

TABLE I. Nonlinear parameters of the resonant system, as used in Eqs. (19) to produce the results illustrated in Figs. 4(c) and 5.

SPM	XPM	DFWM
$r_{\text{SPM},1} = 3.47$	$r_{\text{XPM},12} = 5.06$	$r_{\text{DFWM},1} = 1.17 - j0.038$
	$r_{\text{XPM},13} = 4.24$	
$r_{\text{SPM},2} = 4.64$	$r_{\text{XPM},21} = 5.71$	$r_{\text{DFWM},2} = 1.32 + j0.042$
	$r_{\text{XPM},23} = 5.20$	
$r_{\text{SPM},3} = 2.47$	$r_{\text{XPM},31} = 3.62$	$r_{\text{DFWM},3} = 0.99 + j0.032$
	$r_{\text{XPM},32} = 3.94$	

of an unstable operating region (appearing due to a system bifurcation), shown as the white area in Fig. 4(b). In that region, a phenomenon commonly referred to as *limit cycles* appears [14,15], resulting in a pulsed-pattern output of the ω_3^{op} wave, despite the continuous wave (CW) feed at ω_1^{op} and ω_2^{op} [inset of Fig. 4(b)]. Limit cycles area is determined by the inability to obtain a solution using the CW version of the CMT equations. The pulsed-pattern output [seen in the inset of Fig. 4(b)] is then identified by solving the dynamic version of the CMT equations.

In an even more realistic treatment, the effect of the nonlinear resonance frequency shifts due to SPM and XPM should be taken into account ($\gamma_{k\ell} \neq 0$ in the CMT framework). Based on the linear eigenvalue simulations, the intensity factors for the various nonlinear effects appearing in the resonant system are calculated and listed in Table I. By substituting these values in Eqs. (19), we can calculate the conversion efficiency of the DFWM process under realistic conditions, Fig. 4(c). Compared to Figs. 4(a) and 4(b), the maximum CE is considerably lower. More specifically, for $P_{\text{in},1} = 1.0P_3 = 0.606$ mW/μm and $P_{\text{in},2} = 0.6P_3 = 0.364$ mW/μm ($P_{\text{in},1} = 3.6$ mW, $P_{\text{in},2} = 2.2$ mW for a reference 3D system that is $\lambda_{\text{SPP}}/2$ wide), one finds the maximum CE being equal to -31.5 dB. This CE drop is due to SPM and XPM shifting the cavity resonances away from the respective operating frequencies, leading to nonzero detuning and, as a consequence, to suboptimal light-cavity coupling.

As a remedy to this problem, we can preshift the operating frequencies of the input waves with respect to the unperturbed resonance frequencies to accommodate for the red-shifting induced by the Kerr effect [13,14]. Naturally, shifting δ_1 and δ_2 inevitably affects δ_3 as dictated by the DFWM frequency condition $\omega_3^{\text{op}} = 2\omega_1^{\text{op}} - \omega_2^{\text{op}}$. Additionally, one should keep in mind that the optimum preshifting is not the same for each pair of $p_{\text{in},1} - p_{\text{in},2}$ since the Kerr-induced nonlinear resonance frequency shift is power dependent [42]. We set $P_{\text{in},1} = 1.0P_3$ and $P_{\text{in},2} = 0.6P_3$, which was the optimum pair for $\delta_1 = \delta_2 = 0$, and seek the combination of δ_1 and δ_2 that further maximizes CE. The results are shown in Fig. 5. Notably, for $\delta_1 = -3.10$ and $\delta_2 = -2.35$ (the star-marked point), a CE of -17.6 dB is obtained, constituting a significant improvement. In fact, we have managed to almost completely compensate for the impairment introduced by the nonlinear resonance frequency shifts, confronting a problem commonly encountered in experimental works [5,7,8,10]. The compensation is not complete since the input power combination leading to maximum CE is different in the presence or absence of
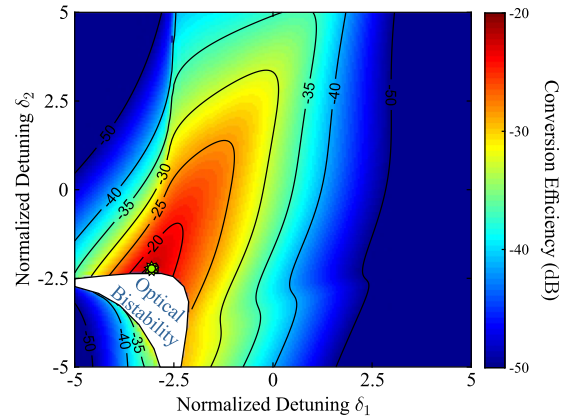
FIG. 5. Conversion efficiency of the DFWM process in the $\delta_1 - \delta_2$ space when all effects are taken into account. The power levels of the input waves are $p_{\text{in},1} = 1.0$ and $p_{\text{in},2} = 0.6$. A maximum CE of -17.6 dB is obtained for $\delta_1 = -3.10$ and $\delta_2 = -2.35$.

SPM/XPM. Thus, the input power pair should be further fine tuned for achieving larger compensation. In addition, there exists a region (marked with white) where optical bistability manifests [initially appearing for [45] $\delta_k < -(1 + r_{Q,k})\sqrt{3}$] and higher CEs are anticipated. Nevertheless, we do not opt for operating in the bistability region since, along with the high-output state, there exists a low-output state where the system may evolve into, negatively affecting the overall performance.

V. CONCLUSION

To summarize, we have developed a rigorous mathematical framework that can analyze single-channel and multichannel nonlinear processes in resonant systems comprising sheet (2D) and bulk materials. Using the proposed framework, we have thoroughly studied degenerate four-wave mixing in a graphene plasmon-polariton standing-wave resonant structure operating in the THz frequency range. More specifically, we have determined the optimum operating point leading to maximum conversion efficiency and numerically identified the different operating regimes (giving rise to optical bistability or limit cycles behavior) appearing when varying the power level of the input waves or their operating frequency. The field enhancement offered by the tightly confined graphene plasmon-polaritons allows for obtaining high-conversion efficiency for the DFWM process, indicating the potential of graphene for on-chip nonlinear photonic functionalities. Specifically for our design, a CE of -17.6 dB (-14.6 dB accounting for idler propagating both in the forward and backward directions) is obtained for input powers of $P_{\text{in},1} = 0.606$ mW/μm and $P_{\text{in},2} = 0.364$ mW/μm, using feeding frequencies with normalized detunings equal to $\delta_1 = -3.10$ and $\delta_2 = -2.35$. Our work paves the way for studying diverse multichannel phenomena (frequency generation, frequency mixing, and parametric amplification) in resonant systems comprising novel 2D materials (graphene, transition metal dichalcogenides, hexagonal boron nitride, black phosphorus, etc.), thus bringing these exciting materials one step closer to practical nonlinear applications.

[1] G. P. Agrawal, *Applications of Nonlinear Fiber Optics*, 2nd ed. (Academic, New York, 2007).

[2] H. Fukuda, K. Yamada, T. Shoji, M. Takahashi, T. Tsuchizawa, T. Watanabe, J. ichi Takahashi, and S. ichi Itabashi, Opt. Express **13**, 4629 (2005).

[3] J. R. Ong, R. Kumar, R. Aguinaldo, and S. Mookherjea, IEEE Photonics Technol. Lett. **25**, 1699 (2013).

[4] S. Lavdas and N. C. Panoiu, Phys. Rev. B **93**, 115435 (2016).

[5] Q. Li, M. Davanço, and K. Srinivasan, Nat. Photonics **10**, 406 (2016).

[6] M. Ferrera, D. Duchesne, L. Razzari, M. Peccianti, R. Morandotti, P. Cheben, S. Janz, D.-X. Xu, B. E. Little, S. Chu, and D. J. Moss, Opt. Express **17**, 14098 (2009).

[7] A. C. Turner, M. A. Foster, A. L. Gaeta, and M. Lipson, Opt. Express **16**, 4881 (2008).

[8] A. Pasquazi, R. Ahmad, M. Rochette, M. Lamont, R. Morandotti, B. E. Little, S. T. Chu, and D. J. Moss, Opt. Express **18**, 3858 (2010).

[9] N. Vermeulen, J. E. Sipe, L. G. Helt, and H. Thienpont, Laser Photonics Rev. **6**, 793 (2012).

[10] J. B. Surya, X. Guo, C.-L. Zou, and H. X. Tang, Optica **5**, 103 (2018).

[11] X. Cui, W. Zhang, S. Serna, C. Alonso-Ramos, D. Marris-Morini, L. Vivien, J.-J. He, and E. Cassan, J. Opt. Soc. Am. B **35**, 636 (2018).

[12] A. Rodriguez, M. Soljačić, J. D. Joannopoulos, and S. G. Johnson, Opt. Express **15**, 7303 (2007).

[13] H. Hashemi, A. W. Rodriguez, J. D. Joannopoulos, M. Soljačić, and S. G. Johnson, Phys. Rev. A **79**, 013812 (2009).

[14] D. M. Ramirez, A. W. Rodriguez, H. Hashemi, J. D. Joannopoulos, M. Soljačić, and S. G. Johnson, Phys. Rev. A **83**, 033834 (2011).

[15] Z. Lin, T. Alcorn, M. Loncar, S. G. Johnson, and A. W. Rodriguez, Phys. Rev. A **89**, 053839 (2014).

[16] A. N. Grigorenko, M. Polini, and K. S. Novoselov, Nat. Photonics **6**, 749 (2012).

[17] S. Psilodimitrakopoulos, L. Mouchliadis, I. Paradisanos, A. Lemonis, G. Kioseoglou, and E. Stratakis, Light-Sci. Appl. **7**, 18005 (2018).

[18] F. Xia, H. Wang, D. Xiao, M. Dubey, and A. Ramasubramaniam, Nat. Photonics **8**, 899 (2014).

[19] Z. Sun, A. Martinez, and F. Wang, Nat. Photonics **10**, 227 (2016).

[20] X. Shi, X. Lin, I. Kaminer, F. Gao, Z. Yang, J. D. Joannopoulos, M. Soljačić, and B. Zhang, Nat. Phys. **14**, 1001 (2018).

[21] N. Kumar, J. Kumar, C. Gerstenkorn, R. Wang, H. Y. Chiu, A. L. Smirl, and H. Zhao, Phys. Rev. B **87**, 121406(R) (2013).

[22] C. Q. Xia, C. Zheng, M. S. Fuhrer, and S. Palomba, Opt. Lett. **41**, 1122 (2016).

[23] B. Jin, T. Guo, and C. Argyropoulos, J. Opt. **19**, 094005 (2017).

[24] C. Beckerleg, T. J. Constant, I. Zeimpekis, S. M. Hornett, C. Craig, D. W. Hewak, and E. Hendry, Appl. Phys. Lett. **112**, 011102 (2018).

[25] S. A. Mikhailov, Europhys. Lett. **79**, 27002 (2007).

[26] S. A. Mikhailov, Phys. Rev. B **90**, 241301(R) (2014).

[27] J. L. Cheng, N. Vermeulen, and J. E. Sipe, New J. Phys. **16**, 053014 (2014).

[28] D. Chatzidimitriou, A. Pitilakis, and E. E. Kriezis, J. Appl. Phys. **118**, 023105 (2015).

[29] Y. Jiang, X. Lin, T. Low, B. Zhang, and H. Chen, Laser Photonics Rev. **12**, 1800049 (2018).

[30] N. Vermeulen, J. L. Cheng, J. E. Sipe, and H. Thienpont, IEEE J. Sel. Top. Quantum **22**, 8100113 (2016).

[31] K. Alexander, N. A. Savostianova, S. A. Mikhailov, B. Kuyken, and D. Van Thourhout, ACS Photonics **4**, 3039 (2017).

[32] T. Gu, N. Petrone, J. F. McMillan, A. Van Der Zande, M. Yu, G. Q. Lo, D. L. Kwong, J. Hone, and C. W. Wong, Nat. Photonics **6**, 554 (2012).

[33] M. Ji, H. Cai, L. Deng, Y. Huang, Q. Huang, J. Xia, Z. Li, J. Yu, and Y. Wang, Opt. Express **23**, 18679 (2015).

[34] T. Christopoulos, O. Tsilipakos, N. Grivas, and E. E. Kriezis, Phys. Rev. E **94**, 062219 (2016).

[35] T. Christopoulos, O. Tsilipakos, and E. E. Kriezis, J. Appl. Phys. **122**, 233101 (2017).

[36] V. G. Ataloglou, T. Christopoulos, and E. E. Kriezis, Phys. Rev. A **97**, 063836 (2018).

[37] J. Bravo-Abad, S. Fan, S. Johnson, J. D. Joannopoulos, and M. Soljačić, J. Lightw. Technol. **25**, 2539 (2007).

[38] H. A. Haus, *Waves and Fields in Optoelectronics* (Prentice-Hall, New Jersey, 1984).

[39] M. Soljačić, M. Ibanescu, S. G. Johnson, Y. Fink, and J. D. Joannopoulos, Phys. Rev. E **66**, 055601(R) (2002).

[40] E. Dremetsika and P. Kockaert, Phys. Rev. B **96**, 235422 (2017).

[41] R. Li, X. Lin, S. Lin, X. Zhang, E. Li, and H. Chen, Carbon **98**, 463 (2016).

[42] O. Tsilipakos, T. Christopoulos, and E. E. Kriezis, J. Lightw. Technol. **34**, 1333 (2016).

[43] S. Fan, W. Suh, and J. D. Joannopoulos, J. Opt. Soc. Am. A **20**, 569 (2003).

[44] X. Zeng and M. A. Popović, Opt. Express **22**, 15837 (2014).

[45] T. Christopoulos, G. Sinatkas, O. Tsilipakos, and E. E. Kriezis, Opt. Quantum Electron. **48**, 128 (2016).